Histopathology

Histopathology 2019, **74**, 1036–1044. DOI: 10.1111/his.13848

Three-dimensional architecture of common benign and precancerous prostate epithelial lesions

Esther I Verhoef,[1] Wiggert A van Cappellen,[1,2] Johan A Slotman,[1,2] Gert-Jan Kremers,[1,2] Patricia C Ewing-Graham,[1] Adriaan B Houtsmuller,[1,2] Martin E van Royen[1,2] & Geert J L H van Leenders[1]

Departments of [1]Pathology, and [2]Optical Imaging Center, Erasmus MC, University Medical Center Rotterdam, Rotterdam, the Netherlands

Date of submission 24 January 2019
Accepted for publication 25 February 2019
Published online *Article Accepted* 28 February 2019

Verhoef E I, van Cappellen W A, Slotman J A, Kremers G-J, Ewing-Graham P C, Houtsmuller A B, van Royen M E & van Leenders G J L H

(2019) *Histopathology* **74**, 1036–1044. https://doi.org/10.1111/his.13848

Three-dimensional architecture of common benign and precancerous prostate epithelial lesions

Aims: Many glandular lesions can mimic prostate cancer microscopically, including atrophic glands, adenosis and prostatic intraepithelial neoplasia. While the characteristic histopathological and immunohistochemical features of these lesions have been well established, little is known about their three-dimensional architecture. Our objective was to evaluate the three-dimensional organisation of common prostate epithelial lesions.

Methods and results: 500 μm-thick punches (n = 42) were taken from radical prostatectomy specimens, and stained with antibodies targeting keratin 8–18 and keratin 5 for identification of luminal and basal cells, respectively. Tissue samples were optically cleared in benzyl alcohol:benzyl benzoate and imaged using a confocal laser scanning microscope. The three-dimensional architecture of peripheral and transition zone glands was acinar, composed of interconnecting and blind-ending saccular tubules. In simple atrophy, partial atrophy and post-atrophic hyperplasia, the acinar structure was attenuated with branching blind-ending tubules from parental tubular structures. Three-dimensional imaging revealed a novel variant of prostate atrophy characterised by large Golgi-like atrophic spaces parallel to the prostate surface, which were represented by thin, elongated tubular structures on haematoxylin and eosin (H&E) slides. Conversely, adenosis lacked acinar organisation, so that it closely mimicked low-grade prostate cancer. High-grade prostatic intraepithelial neoplasia displayed prominent papillary intraluminal protrusions but retained an acinar organisation, whereas intraductal carcinoma predominantly consisted of cribriform proliferations with either spheroid, ellipsoid or complex interconnecting lumens.

Conclusions: While various prostate epithelial lesions might mimic malignancy on H&E slides, their three-dimensional architecture is acinar and clearly different from the tubular structure of prostate cancer, with adenosis as an exception.

Keywords: prostate, three-dimensional imaging, tissue clearing

Introduction

The vast majority of prostate cancers are diagnosed on histopathological slides of transrectal or transperineal biopsies prompted by an elevated prostate-specific antigen (PSA) serum level or lower urinary tract symptoms. Prostate cancer (PCa) diagnosis is usually straightforward, and in most cases does not require supportive immunohistochemical staining. However, immunohistochemistry with keratin 5, p63, alpha-methylacyl-CoA racemase (AMACR) and ETS-related gene (ERG) antibodies can be used for accurate

Address for correspondence: E I Verhoef, Department of Pathology, Erasmus MC, University Medical Center Rotterdam, PO Box 2040, 3000 CA Rotterdam, the Netherlands. e-mail: e.verhoef@erasmusmc.nl

diagnosis of small tumour foci and for distinction from benign glandular mimics.[1–5]

Many glandular lesions can resemble PCa.[6,7] Glandular atrophy most frequently enters the differential diagnosis with conventional PCa.[8] Atypical adenomatous hyperplasia, or adenosis, and high-grade prostatic intraepithelial neoplasia are other common lesions with resemblance to PCa. While immunohistochemical stains can aid decision-making, the classification of a small number of lesions remains uncertain, and these have been referred to as atypical small acinar proliferations.[9]

Histopathological evaluation is generally performed by microscopic analysis of 4–5 μm thick haematoxylin and eosin (H&E) stained tissue slides. Our knowledge of histopathology and conventional diagnostic criteria is therefore entirely based on two-dimensional features. Little is known about the three-dimensional (3D) architecture of normal prostate glands, benign epithelial lesions and PCa. Recent developments in the field of optical tissue clearing allow for sensitive deep fluorescent imaging of tissue specimens. While these techniques have mostly been used for studying *in-vitro* and animal models, we have recently adapted the methodology for use on formalin-fixed, paraffin-embedded prostate tissues. This allows 3D imaging of specific regions of interest.[10] In this study we aimed to clarify the 3D architecture of the most common benign and precancerous prostate glandular lesions.

Materials and Methods

CASE SELECTION

A selection was made of archival formalin-fixed, paraffin-embedded radical prostatectomy specimens from patients who had undergone radical prostatectomy at the Erasmus Medical Center in Rotterdam between 2012 and 2017. These tissue specimens were fixed in neutral-buffered formalin and routinely processed for histopathological evaluation. A urogenital pathologist (G.v.L.) indicated regions of interest on 5-μm-thick H&E-stained tissue slides. In total, 42 areas from 32 patients were used. These areas included glands from the normal peripheral (n = 3) and transition zone (n = 7), simple atrophy (n = 6), cystic atrophy (n = 5), post-atrophic hyperplasia (n = 1), partial atrophy (n = 2), adenosis (n = 4), high-grade prostatic intraepithelial neoplasia (n = 9) and intraductal carcinoma (n = 5), as well as one prostate cancer case for reference purposes. The use of tissue samples for scientific purposes was approved by the institutional Medical Research Ethics Committee (MEC-2011-295, MEC-2011-296). Samples were used in accordance with the 'Code for Proper

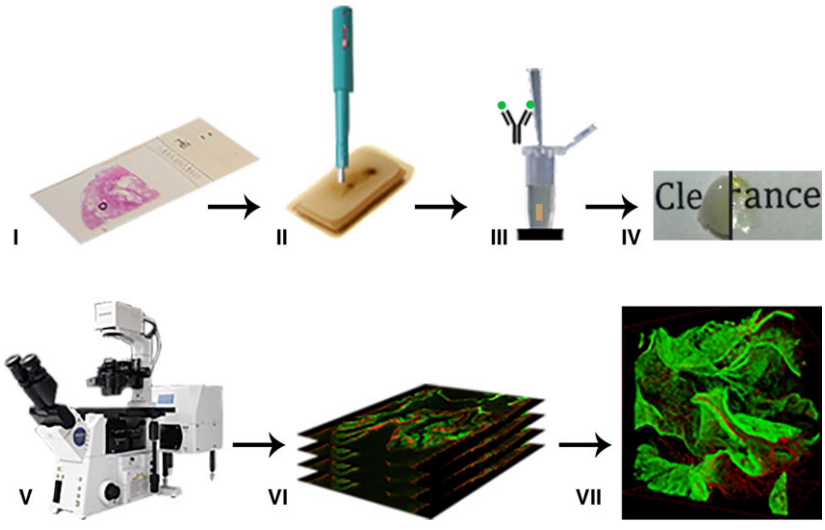

Figure 1. Work-flow for three-dimensional (3D) imaging of formalin-fixed, paraffin-embedded tissues. (i) Tissue selection on haematoxylin and eosin (H&E) slides, (ii) tissue punching from corresponding blocks, in which the H&E slide was directly adjacent to the top of the cylindrical biopsy punch, (iii) incubation with fluorescently labelled antibodies, (iv) optical tissue clearing, (v) fluorescent confocal imaging, (vi) stacking of confocal images and visual Z-stack analysis and (vii) image processing and 3D rendering.

Secondary Use of Human Tissue in The Netherlands', as developed by the Dutch Federation of Medical Scientific Societies (FMWV, version 2002, updated 2011).

IMMUNOFLUORESCENT STAINING AND OPTICAL CLEARING

The total work-flow is depicted in Figure 1. Tissue punches from the regions of interest were taken from the corresponding paraffin blocks using a 500-μm diameter needle (Estigen, Tartu, Estonia), resulting in 3–4-mm-long cylindrical tissue cores with a diameter of 500 μm. Immunofluorescent staining was performed according to an adapted iDISCO protocol, as described previously.[10,11] In short, punches were dewaxed and this was followed by an autofluorescence blocking step. Thereafter the tissue punches were gradually rehydrated and incubated with keratin 5 and keratin 8/18 targeting antibodies (1:150; EP1601Y; Abcam, Cambridge, UK and 1:75; MS-743; Immunologic, Duiven, the Netherlands). These were visualised with secondary fluorescent Alexa 514- and Alexa 647-labelled antibodies (1:200; Life Technologies, Bleiswijk, the Netherlands). After dehydration in methanol, an optical clearing step was performed by immersing the tissue in benzyl-alcohol:benzyl benzoate until optical transparency was achieved. Samples were stored at 4°C in the dark until imaging.

SAMPLE IMAGING

Confocal fluorescent imaging was performed with an upright Leica SP5 confocal microscope fitted with a 1.95-mm working distance 20× NA1.0 APO water dipping objective (Leica Microsystems GmbH, Wetzlar, Germany). A 488-nm Argon and a 633-nm HeNe laser were used to record two-dimensional Z-stack images, resulting in 300–600 images per sample with a 0.72 × 0.72-μm pixel size and 1–3-μm step-size. Thereafter, Z-stacks were de-convoluted using a theoretical point-spread-function (PSF) in the Huygens Professional software (SVI, Hilversum, the Netherlands). Image processing and 3D rendering was performed with Fiji (ImageJ 1.49s) and Amira (version 5.5.0; ThermoFisher Scientific, Waltham, MA, USA) software. For 3D renderings as depicted in this paper, Z-stacks were loaded in Amira after which we applied combined surface rendering and volume rendering with standard settings.[12] Total Z-stacks and 3D renderings were 739 × 739 μm in size with a 500–1000-μm depth.

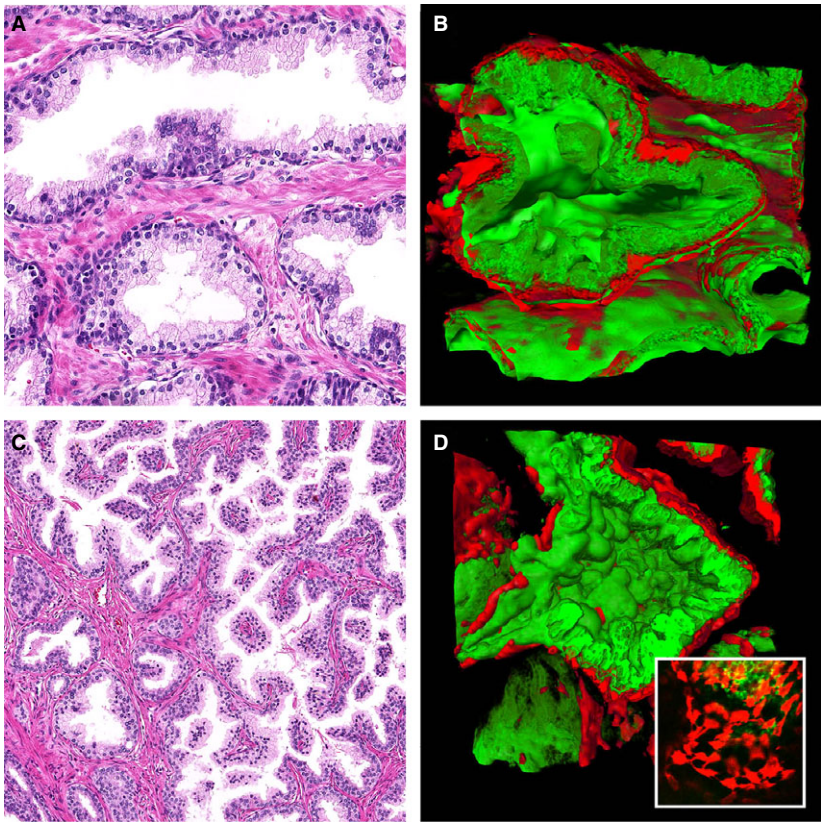

Figure 2. Peripheral zone (**A**) haematoxylin and eosin (H&E) slide and (**B**) three-dimensional (3D) rendering, showing large saccular tubules with interconnections, variable width and continuous layer of basal cells. Transition zone (**C**) H&E slide and (**D**) 3D rendering with abundant presence of epithelial protrusions. Inset: 3D rendering of a tubule ending with scattered basal cells showing slender cytoplasmic interconnections. Green keratin 8/18 and red keratin 5 immunostaining in 3D renderings.

PATHOLOGICAL EVALUATION AND STATISTICAL ANALYSIS

Visual analysis and tubule measurement was performed on Z-stacks as well as on corresponding rendered 3D reconstructions. Benign and precancerous lesions could be identified by keratin 8/18-positive luminal cells surrounded by keratin 5-positive basal cells, whereas PCa lacked the basal cell layer. The outer edges of the epithelial lesions were measured in three to five separate slides per image and three to 10 individual epithelial structures per slide, depending on the lesion. This resulted in 15–50 measurements per tissue sample. Glandular diameters were calculated as the average of all measurements for that lesion. Mean diameters were compared with a Student's *t*-test using the Statistical Package for Social Sciences (SPSS, version 24; IBM, Chicago, IL, USA).

Results

PERIPHERAL AND TRANSITION ZONE

On routine H&E slides, peripheral zone glands consist of round, oval or slightly irregular glands with local small intraluminal protrusions with a fibrovascular core. Three-dimensional imaging revealed that peripheral zone glands had an acinar organisation, which was composed of interconnecting blind-ending saccular tubules with a mean diameter of 151 μm [standard deviation (SD) 55 μm, Figure 2A,B]. These tubules did not show a hierarchical pattern, and a clear distinction between distal saccular structures and more central ducts was lacking (Video S1). The scant intraluminal protrusions represented finger-like structures rather than longitudinal plicae. The 3D architecture of transition zone glands was similar to peripheral zone glands, with a mean tubular diameter of 165 μm (SD = 75 μm). The most prominent difference was the abundance of intraluminal protrusions (Figure 2C,D, Video S2). Most acini were entirely surrounded by a compact sheet of keratin 5-positive basal cells. However, regions of regularly spaced basal cells with slender interconnecting cytoplasmic sprouts were also identified, usually at tubule endings (Figure 2D, inset). The interconnecting saccular structures were more abundantly present in adenomatous hyperplastic nodules.

ATROPHY

Four different variants of prostate glandular atrophy are recognised on H&E slides: simple atrophy, simple atrophy with cyst formation, partial atrophy and

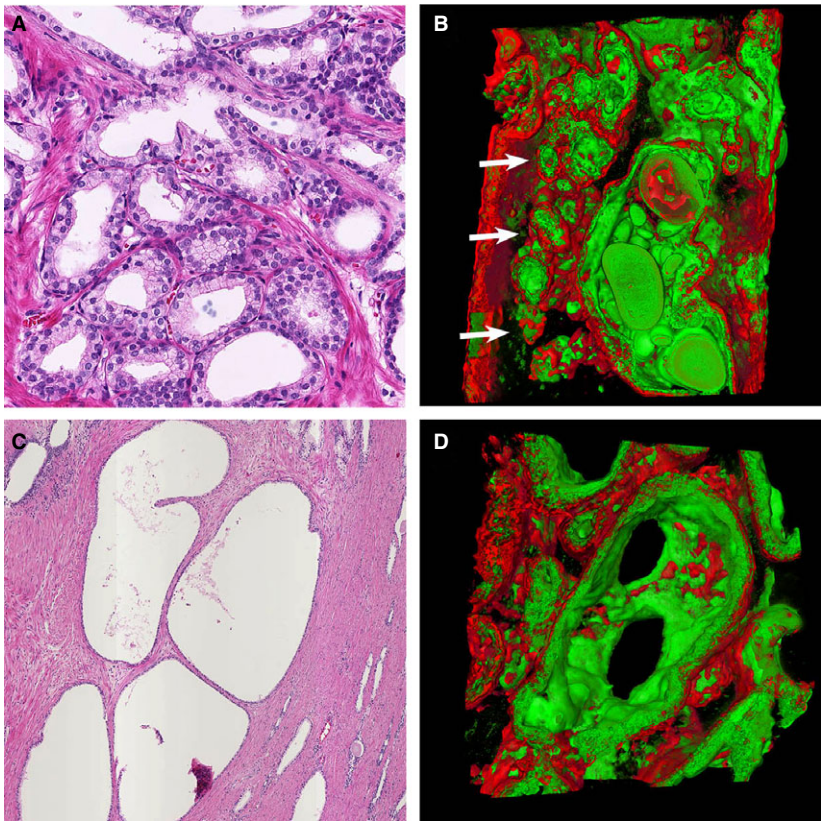

Figure 3. Simple atrophy (**A**) haematoxylin and eosin (H&E) slide and (**B**) three-dimensional (3D) rendering with acini of short saccular tubules (arrows) interconnecting with a dilated gland filled with corpora amylacea. Cystic atrophy (**C**) H&E slide and (**D**) 3D rendering with large dilated glands in connection with adjacent glands, represented by dark oval openings. Green keratin 8/18 and red keratin 5 immunostaining in 3D renderings.

post-atrophic hyperplasia.[13] The overall 3D glandular architecture of simple atrophy was tubular, emphasising the prostatic acinar organisation of central tubules with branching and blind-ending tubules. The tubules had a mean diameter of 52 μm (SD = 16 μm) and were surrounded by a continuous sheet of basal cells (Figure 3A,B). In some cases connections were seen between atrophic tubules and larger glands with corpora amylacea (Video S3). Cystic atrophy consisted of dilated glands with a mean diameter of 202 μm (SD = 118 μm), significantly larger than the acini of the peripheral or transition zone ($P < 0.001$). Here, the overall acinar organisation was retained with the presence of dilated saccular or tubular outpouchings from the cyst (Figure 3C,D, Video S4). In some cases, large corpora amylacea could be seen in the cystic tubules. Post-atrophic hyperplasia had a similar acinar organisation in which the difference between central and branching blind-ending tubules could be more clearly appreciated (Figure 4A,B, Video S5). Partially atrophic tubules displayed an acinar organisation, with basal cells typically lacking around a significant part of the lesion (Figure 4C,D, Video S6). Although four

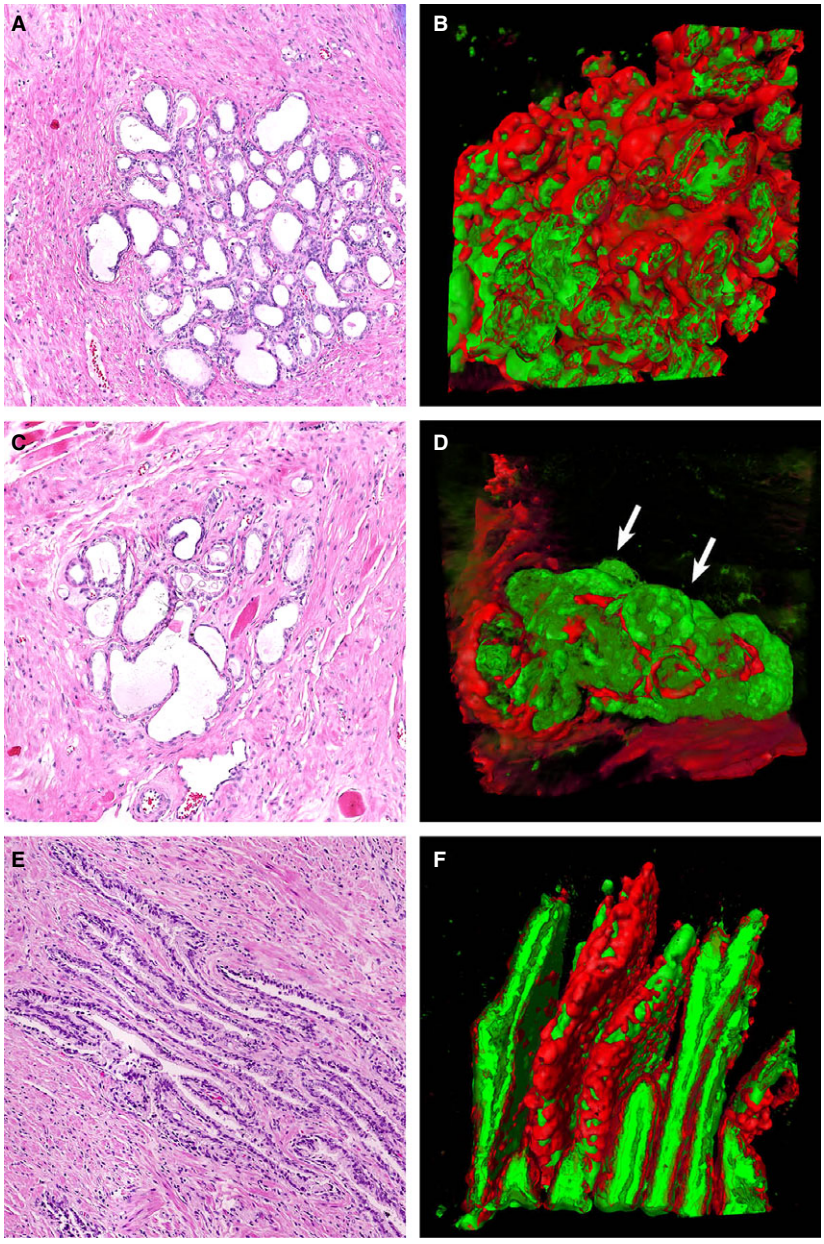

Figure 4. Post-atrophic hyperplasia (**A**) haematoxylin and eosin (H&E) slide and (**B**) three-dimensional (3D) rendering with an acinus of short saccular tubules. Partial atrophy (**C**) H&E slide and (**D**) 3D rendering with an irregular acinus of short tubules with large areas lacking a basal cell layer (arrows). Golgi-like atrophy (**E**) H&E slide and (**F**) 3D rendering, showing parallel longitudinal ellipsoid slit-like structures in an arrangement that resembles the Golgi apparatus. Green keratin 8/18 and red keratin 5 immunostaining in 3D renderings.

atrophic patterns have been defined previously on H&E slides, 3D reconstruction clearly revealed an additional pattern. This pattern consisted of parallel large slit-like ellipsoid spaces with few interconnections, resulting in a Golgi-like organisation (Figure 4E,F, Video S7). On H&E slides this atrophic variant appeared as longitudinally sectioned tubules at the dorsolateral sides of the prostate.

ADENOSIS

On H&E slides, adenosis can closely mimic Gleason score 6 PCa, with closely packed round glands lined with slightly atypical luminal epithelial cells, often with intraluminal secretions and crystalloids. Three-dimensional renderings showed that adenosis was composed of small- to medium-sized tubules with a mean diameter of 71 μm (SD = 33 μm). These tubules were smaller than transition zone gland tubules ($P < 0.001$) and discontinuously covered with basal cell clusters. The tubules were branching to such an extent that no obvious acinar organisation could be appreciated (Figure 5A,B, Video S8). For comparison, we have included a sample of Gleason score 6 prostate adenocarcinoma consisting of tubules with rare interconnections. These formed a disorganised network composed of luminal cells only and had no basal cell layer (Figure 5C,D). For a complete and comprehensive description of the 3D architecture of prostate adenocarcinoma growth patterns, we refer to our previous study.[14]

HIGH-GRADE PROSTATIC INTRA-EPITHELIAL NEOPLASIA

On 3D imaging, high-grade prostatic intraepithelial neoplasia retained an acinar organisation with short tubular and saccular outpouchings of 171 μm (SD = 76 μm). The diameter of these structures was not statistically different from peripheral or transition zone glands ($P = 0.072$). Most acini were lined by a compact sheet of basal cells; however, there were only scattered basal cells present in some regions. Papillary intraluminal finger-like protrusions lined by luminal cells were abundant (Figure 6A,B). High-grade prostatic intraepithelial neoplasia was connected to adjacent pre-existent glands in 3D reconstructions (Video S9).

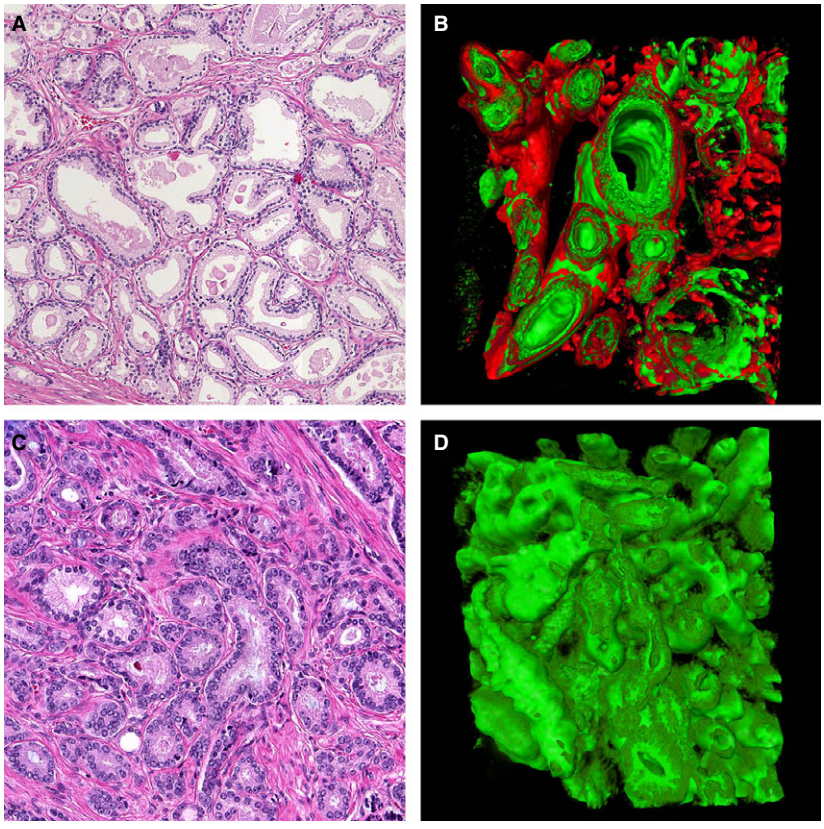

Figure 5. Adenosis (**A**) haematoxylin and eosin (H&E) slide and (**B**) three-dimensional (3D) rendering with tubular architecture, lacking a clear branching acinar structure. Gleason grade 3 prostate cancer (**C**) H&E slide and (**D**) 3D rendering displaying a network of interconnecting tubules. Green keratin 8/18 and red keratin 5 immunostaining in 3D renderings.

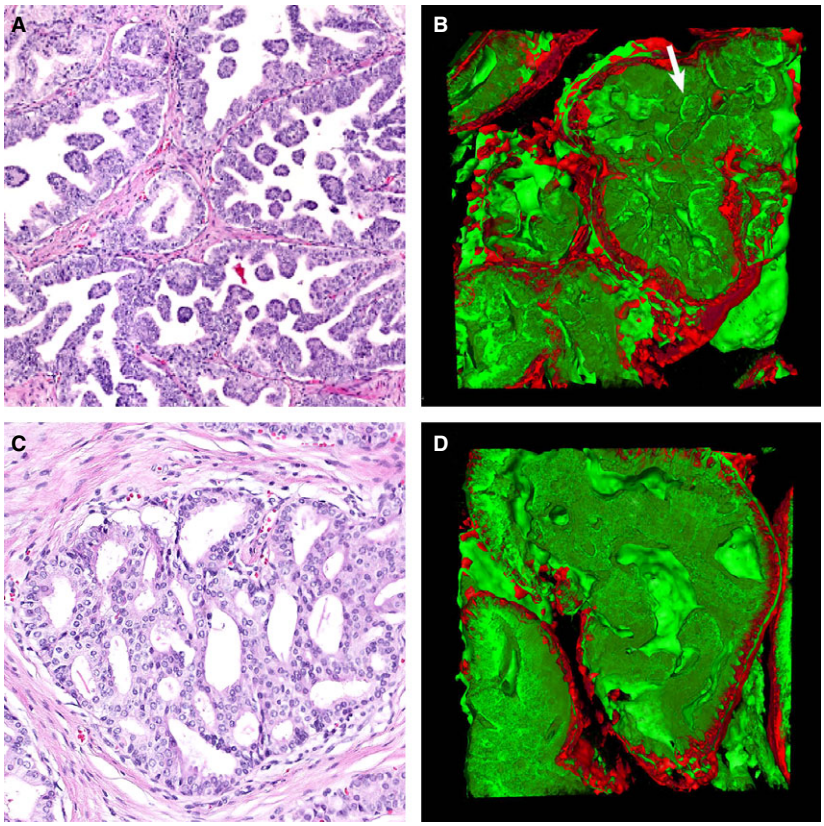

Figure 6. High-grade prostatic intraepithelial neoplasia (PIN) (**A**) haematoxylin and eosin (H&E) slide and (**B**) three-dimensional (3D) rendering with saccular architecture and abundant papillary protrusions (arrow). Intraductal carcinoma of the prostate (**C**) H&E slide and (**D**) 3D rendering with gland spanning liminal epithelial proliferation with irregular interconnecting luminal spaces. Green keratin 8/18 and red keratin 5 immunostaining in 3D renderings.

INTRADUCTAL CARCINOMA

Intraductal carcinoma of the prostate predominantly consists of malignant cribriform or solid epithelial proliferations spanning the entire lumen of dilated pre-existent glands. Three-dimensional rendering revealed an intact distended acinar architecture of pre-existent glands with a mean diameter of 153 μm (SD = 92 μm), filled with a solid or cribriform mass of luminal epithelial cells. In cribriform lesions, lumens were either small spheroid, ellipsoid or complex interconnecting spaces with rounded or sharp endings (Figure 6C,D, Video S10). While intraductal carcinoma is generally larger than high-grade prostate intraepithelial neoplasia, we selected relatively small lesions for 3D visualisation because of confocal field view limitations. The most prominent difference with high-grade prostatic intraepithelial neoplasia was the presence of lumen-spanning epithelial proliferations.

Discussion

In this study we have provided a comprehensive overview of the 3D architecture of common benign prostate epithelial lesions which might mimic PCa on H&E slides. We demonstrated that peripheral and transition zone glands have an acinar organisation, with interconnecting saccular blind-ended tubules without clear hierarchical arrangement. This basic acinar organisation was retained in adenomatous hyperplasia and high-grade prostatic intraepithelial neoplasia and was emphasised in atrophy. We were able to identify a novel atrophic variant by 3D microscopy, consisting of large flat ellipsoid spaces with a Golgi-like appearance parallel to the prostate dorsolateral capsule. This atrophic variant showed longitudinally sectioned glands on H&E slides, which were located in the peripheral zone of the prostate. Interestingly, adenosis was the only variant showing a tubular instead of an acinar organisation, closely mimicking Gleason score 6 PCa.

The differential diagnoses of PCa, including atrophy, adenosis and prostatic intraepithelial neoplasia, have been described extensively in various studies.[15–17] Although their histopathological and immunohistochemical features are well known, little is known about the underlying 3D architecture of these benign mimics.[18,19] Benign and malignant prostate lesions can show overlapping morphological features on H&E slides.

However, we found that the 3D architecture of most benign epithelial lesions was entirely different.[10,14] For instance, simple and partial atrophy might closely resemble PCa on H&E and immunohistochemical stained slides, showing partial loss of basal cells.[8] However, their 3D structure showed that these lesions clearly retain an acinar organisation, which is disrupted in PCa.[10]

Simple atrophy, partial atrophy and post-atrophic hyperplasia most clearly revealed the basic acinar organisation of the prostate, showing branching of a central tubule into small blind-ended tubules. Peripheral and transition zone glands were also organised in an acinar fashion; however, this was less obvious owing to the larger size of these glands and to the presence of papillary protrusions. Atrophic tubules were sometimes connected to slightly distended glands with numerous corpora amylacea, suggesting glandular obstruction as the cause of cystic atrophy. Importantly, we found the presence of large slit-like atrophic glands with a Golgi-like 3D organisation which, to our knowledge, has not been reported previously. We hypothesise that these structures are the result of compression of pre-existent glands, for instance by benign hyperplastic nodules. However, the dynamic pathophysiology of these benign glandular lesions remains to be elucidated.

Adenosis was the only lesion in this study that showed a 3D architecture with non-hierarchical interconnecting tubules, reminiscent of Gleason score 6 PCa. While most other prostatic lesions could be discriminated from PCa by their 3D organisation, the presence of basal cells was the only distinguishing feature in adenosis. The similarity between the 3D growth of adenosis and PCa Gleason grade 3 raises the question of whether adenosis and PCa are related. Despite detection of rare molecular aberrations in adenosis it is different from PCa at the molecular level; for instance, there is complete absence of *TMPRSS2:ERG* fusions in adenosis.[20–23] Although adenosis is not a malignant proliferation, it may share aberrant activation of molecular pathways involved in 3D glandular expansion with low-grade PCa.

A strong point of the current study was the use of intact tissue samples from archival prostate specimens. This facilitated selection of specific regions-of-interest for 3D renderings. Imaging of small intact tissue samples prevents alignment artefacts that could occur when using many consecutively cut and stacked slides. However, the use of fluorescently labelled antibodies to distinguish between luminal and basal epithelial cells restricts the potential sample volume to be visualized, owing to limited antibody penetration, especially in compact glandular structures. Therefore, 3D imaging of larger areas was not feasible using the current protocol, which is a disadvantage compared to other 3D imaging techniques such as registration of serial sections.[24] In addition, image analysis is time-consuming, and this meant that we were able to evaluate only a limited number of tissue samples, not covering the entire range of benign prostate epithelial lesions.

In conclusion, long-distance confocal microscopy and optical tissue clearing can be used to comprehensively visualise the unique 3D architecture of benign epithelial lesions of the prostate. While various lesions might mimic malignancy on routine tissue slides, we found that their 3D architecture is mostly entirely different from PCa. Finally, 3D imaging can be helpful in elucidating the pathophysiology of benign prostate glandular lesions.

Conflicts of interest

The authors declare no conflicts of interest.

References

1. Boran C, Kandirali E, Yilmaz F, Serin E, Akyol M. Reliability of the 34betae12, keratin 5/6, p63, bcl-2, and amacr in the diagnosis of prostate carcinoma. *Urol. Oncol.* 2011; **29**; 614–623.
2. Dabir PD, Ottosen P, Hoyer S, Hamilton-Dutoit S. Comparative analysis of three- and two-antibody cocktails to amacr and basal cell markers for the immunohistochemical diagnosis of prostate carcinoma. *Diagn. Pathol.* 2012; **7**; 81.
3. Martens MB, Keller JH. Routine immunohistochemical staining for high-molecular weight cytokeratin 34-beta and alpha-methylacyl coa racemase (p504s) in postirradiation prostate biopsies. *Mod. Pathol.* 2006; **19**; 287–290.
4. Molinie V, Herve JM, Lugagne PM, Lebret T, Botto H. Diagnostic utility of a p63/alpha-methyl coenzyme a racemase (p504s) cocktail in ambiguous lesions of the prostate upon needle biopsy. *BJU Int.* 2006; **97**; 1109–1115.
5. Shah RB, Zhou M, LeBlanc M, Snyder M, Rubin MA. Comparison of the basal cell-specific markers, 34betae12 and p63, in the diagnosis of prostate cancer. *Am. J. Surg. Pathol.* 2002; **26**; 1161–1168.
6. Kowalewski A, Szylberg L, Skorczewska A, Marszalek A. Diagnostic difficulties with atrophy, atypical adenomatous hyperplasia, and atypical small acinar proliferation: a systematic review of current literature. *Clin. Genitourin. Cancer* 2016; **14**; 361–365.
7. Zhou M. High-grade prostatic intraepithelial neoplasia, pin-like carcinoma, ductal carcinoma, and intraductal carcinoma of the prostate. *Mod. Pathol.* 2018; **31**; S71–S79.
8. Herawi M, Parwani AV, Irie J, Epstein JI. Small glandular proliferations on needle biopsies: most common benign mimickers of prostatic adenocarcinoma sent in for expert second opinion. *Am. J. Surg. Pathol.* 2005; **29**; 874–880.
9. Al Diffalha S, Shaar M, Barkan GA *et al.* Immunohistochemistry in the workup of prostate biopsies: frequency, variation and appropriateness of use among pathologists practicing at an academic center. *Ann. Diagn. Pathol.* 2017; **27**; 34–42.

10. van Royen ME, Verhoef EI, Kweldam CF *et al.* Three-dimensional microscopic analysis of clinical prostate specimens. *Histopathology* 2016; **69**; 985–992.
11. Renier N, Wu Z, Simon DJ *et al.* iDisco: a simple, rapid method to immunolabel large tissue samples for volume imaging. *Cell* 2014; **159**; 896–910.
12. Schindelin J, Arganda-Carreras I, Frise E *et al.* Fiji: an open-source platform for biological-image analysis. *Nat. Methods* 2012; **9**; 676–682.
13. De Marzo AM, Platz EA, Epstein JI *et al.* A working group classification of focal prostate atrophy lesions. *Am. J. Surg. Pathol.* 2006; **30**; 1281–1291.
14. Verhoef EI, van Cappellen WA, Slotman JA *et al.* Three-dimensional analysis reveals two major architectural subgroups of prostate cancer growth patterns. *Mod. Pathol.* 2019. https://doi.org/10.1038/s41379-019-0221-0.
15. Berney DM, Fisher G, Kattan MW *et al.* Pitfalls in the diagnosis of prostatic cancer: retrospective review of 1791 cases with clinical outcome. *Histopathology* 2007; **51**; 452–457.
16. Epstein JI. Diagnosis of limited adenocarcinoma of the prostate. *Histopathology* 2012; **60**; 28–40.
17. Netto GJ, Epstein JI. Benign mimickers of prostate adenocarcinoma on needle biopsy and transurethral resection. *Surg. Pathol. Clin.* 2008; **1**; 1–41.
18. Helpap B. Differential diagnosis of glandular proliferations in the prostate. A conventional and immunohistochemical approach. *Virchows Arch.* 1998; **433**; 397–405.
19. Srigley JR. Benign mimickers of prostatic adenocarcinoma. *Mod. Pathol.* 2004; **17**; 328–348.
20. Bettendorf O, Schmidt H, Eltze E *et al.* Cytogenetic changes and loss of heterozygosity in atypical adenomatous hyperplasia, in carcinoma of the prostate and in non-neoplastic prostate tissue using comparative genomic hybridization and multiplex-PCR. *Int. J. Oncol.* 2005; **26**; 267–274.
21. Doll JA, Zhu X, Furman J *et al.* Genetic analysis of prostatic atypical adenomatous hyperplasia (adenosis). *Am. J. Pathol.* 1999; **155**; 967–971.
22. Cheng L, Davidson DD, Maclennan GT *et al.* Atypical adenomatous hyperplasia of prostate lacks TMPRSS2–ERG gene fusion. *Am. J. Surg. Pathol.* 2013; **37**; 1550–1554.
23. Green WM, Hicks JL, De Marzo A, Illei PP, Epstein JI. Immunohistochemical evaluation of TMPRSS2–ERG gene fusion in adenosis of the prostate. *Hum. Pathol.* 2013; **44**; 1895–1901.
24. Tolkach Y, Thomann S, Kristiansen G. 3D-reconstruction of prostate cancer architecture with serial immunohistochemical sections: hallmarks of tumour growth, tumour compartmentalization and implications for grading and heterogeneity. *Histopathology* 2018; **72**; 1051–1059.

Supporting Information

Additional Supporting Information may be found in the online version of this article:

Video S1. Three-dimensional rendering of peripheral zone with large interconnecting saccular tubules of varying width and a continuous layer of basal cells. Original magnification 20×, green Keratin 8/18 and red Keratin 5 immunostaining.

Video S2. Three-dimensional rendering of transition zone with abundant presence of epithelial protrusions. Original magnification 20×, green Keratin 8/18 and red Keratin 5 immunostaining.

Video S3. Z-stack of simple atrophy with saccular glands (arrows) and putative tubular obstruction by corpora amylacea. The circle indicates interconnection between a dilated gland filled with corpora amylacea on the right side and atrophic glands on the left side. Original magnification 20×, green Keratin 8/18 and red Keratin 5 immunostaining.

Video S4. Three-dimensional rendering of cystic atrophy with large dilated glands interconnecting to the adjacent glands, shown here as two oval dark spaces. Original magnification 20×, green Keratin 8/18 and red Keratin 5 immunostaining.

Video S5. Z-stack of post-atrophic hyperplasia showing an acinar architecture with small branching blind-ending tubules. Original magnification 20×, green Keratin 8/18 and red Keratin 5 immunostaining.

Video S6. Z-stack of partial atrophy with an irregular acinar architecture of short blind-ending tubules and large areas lacking a basal cell layer. Original magnifications 20×, green Keratin 8/18 and red Keratin 5 immunostaining.

Video S7. Three-dimensional rendering of Golgi-like atrophy, showing parallel longitudinal ellipsoid glandular spaces resembling the Golgi-apparatus. Original magnification 20×, green Keratin 8/18 and red Keratin 5 immunostaining.

Video S8. Three-dimensional rendering of adenosis consisting of tubules without clear acinar organization, closely mimicking the structure of Gleason pattern 3 prostate cancer. Original magnification 20×, green Keratin 8/18 and red Keratin 5 immunostaining.

Video S9. Z-stack of high-grade prostate intraepithelial neoplasia with saccular architecture and abundant papillary protrusions. Original magnification 20×, green Keratin 8/18 and red Keratin 5 immunostaining.

Video S10. Z-stack of intraductal carcinoma of the prostate with gland spanning epithelial proliferations and irregular interconnecting luminal spaces. Original magnification 20×, green Keratin 8/18 and red Keratin 5 immunostaining.

